FUNDAMENTALS & APPLICATIONS

CHEMELECTROCHEM

ANALYSIS & CATALYSIS, BIO & NANO, ENERGY & MORE

Accepted Article

Title: The interphase electrochemical characteristics of the cobaltosic oxide in organic electrolyte by Bode plots: double layer capacitance and pseudocapacitance

Authors: Yinsheng Xu, Shengping Wang, Huiling Peng, Zhigao Yang, Darren Martin, Andreas Bund, Ashok Nanjundan, and Yusuke Yamauchi

To be cited as: *ChemElectroChem* 10.1002/celc.201900289

Link to VoR: http://dx.doi.org/10.1002/celc.201900289

A Journal of

ChemPubSoc Europe

WILEY-VCH

www.chemelectrochem.org

The interphase electrochemical characteristics of the cobaltosic oxide in organic electrolyte by Bode plots: double layer capacitance and pseudocapacitance

Yinsheng Xu,[a] Shengping Wang,*[a] Huiling Peng,[a] Zhigao Yang,[a] Darren J. Martin,[b] Andreas Bund,[c] Ashok Kumar Nanjundan[b] and Yusuke Yamauchi*[b, d]

[a] Y. Xu, Prof. S. Wang, H. Peng, Dr. Z. Yang
Faculty of Materials Science and Chemistry, China University of Geosciences, Wuhan 430074, China
E-mail: spwang@cug.edu.cn

[b] Prof. D. J. Martin, Dr. A. K. Nanjundan, Prof. Y. Yamauchi
School of Chemical Engineering & Australian Institute for Bioengineering and Nanotechnology (AIBN), The University of Queensland, Brisbane, QLD 4072, Australia
E-mail: y.yamauchi@uq.edu.au

[c] Prof. A. Bund
Fakultät für Elektrotechnik und Informationstechnik, Fachgebiet Elektrochemie und Galvanotechnik, Technische Universität Ilmenau, Gustav-Kirchhoff-Straße 6 (Arrheniusbau), 98693 Ilmenau, Germany

[d] Prof. Y. Yamauchi
International Center for Materials Nanoarchitectonics (MANA), National Institute for Materials Science (NIMS), 1-1 Namiki, Tsukuba, Ibaraki 305-0044, Japan
E-mail: y.yamauchi@uq.edu.au

Abstract:

Pseudocapacitive behavior is usually observed in transition metal oxide anodes for lithium ion batteries, such as Co_3O_4. It is necessary to develop electrochemical technologies for clarifying the properties of the pseudocapacitance in the electrode reactions, as the understanding and controllable application of pseudocapacitances benefits the development of electrode materials with multi-storage mechanisms for lithium ion batteries. With this purpose, in this work, electrode processes are divided into 4 component parts with corresponding equivalent circuit diagrams used to emphasize the pseudocapacitive behavior of Co_3O_4. After analyzing the properties of Bode plots in the whole frequency range (10^{-2}~10^5 Hz), phase-angle Bode plots are demonstrated to be suitable for revealing the pseudocapacitance for Co_3O_4 at a certain state. In addition, $C = 1/(\omega Z_{Im})$ is utilized to determine the magnitude of the pseudocapacitance and double layer capacitance. For Co_3O_4 in the fully charged state (3 V vs. Li^+/Li), the pseudocapacitance and double layer capacitance are approximately 180.28 μF cm^{-2} and 1.32 μF cm^{-2}, respectively. Therefore, the goal of monitoring pseudocapacitive behavior for a transition metal oxide anode such as Co_3O_4 in a certain state without the influence of double layer capacitance and faradic processes controlled by solid phase diffusion is realized using Bode plots, greatly promoting the understanding and controllable application of pseudocapacitance.

1. Introduction:

Pseudocapacitance is a type of electrochemical phenomenon that differs from a faradic process controlled by solid phase diffusion, which has been discussed in previous reports for lithium ion batteries.[1-4] Pseudocapacitance involves charge storage based on continuous, fast, and reversible redox reactions occurring at the surface of electrode materials.[5-8] Commonly, in a certain battery system, there is always some charge stored via non-faradaic double layer capacitance, which typically ranges between 10 and 50 μF cm^{-2} in aqueous electrolytes and even lower in nonaqueous solvents.[9] Compared with double layer capacitance, the charge density stored with pseudocapacitance is several times higher.[3] Apart from the difference in capacitance values, the majority of the charge is stored via a faradaic process controlled by solid phase diffusion. There are 3 possible sources for the capacities (charge storage) of electrode materials. Among all sources, the pseudocapacitive contribution in transition metal oxides was not only demonstrated to show differential capacity (dQ/dV) curves[10] but also proven to become increasingly important,[3-5, 11-15] which resulted in reversible capacities exceeding the theoretical value for Co_3O_4,[16-25] Fe_2O_3,[26-30] RuO_2[31] and so forth. Thus, clarifying the properties for the pseudocapacitance such as the intensity turns out to be essential at least for the explanation of overflowing theoretical capacities.

However, pseudocapacitance properties can be determined precisely only under the circumstances of a pseudocapacitance that is separate from any faradic process controlled by solid phase diffusion after ruling out double layer capacitance. Unfortunately, it is difficult to electrochemically separate out pseudocapacitance from faradic processes controlled by solid phase diffusion when they coexist with each other, as they both can contribute to the charge storage within a certain electrochemical window.[3, 32] Moreover, it is also more difficult to distinguish the double layer capacitance and pseudocapacitance as they both possess capacitive properties.[3] Thus, an electrochemical technique that can be used to clearly characterize pseudocapacitance is urgently needed for better understanding and controllable application of pseudocapacitances as well as the development of electrode materials with multi-storage mechanisms for lithium ion batteries.

Electrochemical impedance spectroscopy (EIS) is one type of classic electrochemical method that is frequently employed to analyze the impedances of electrochemical processes for electrodes. EIS results are mainly expressed through two different plots with Nyquist plots and Bode plots. Nyquist plots can almost directly reveal the impedances and their differences for different parts of the

electrode reactions, which is very convenient and efficient.[33] While Bode plots, which are rarely discussed when dealing with problems associated with electrodes, possess much more information, including the pseudocapacitance of a certain electrode.

In this report, the electrochemical processes of a Co_3O_4 electrode in lithium ion batteries are divided into at least 4 parts, as illustrated in Fig. 1, including processes that obey Ohm's law, a faradic process controlled by solid phase diffusion, a pseudocapacitive process and other possible phenomena. An equivalent circuit diagram is also built to determine each component of the electrode processes. Characterization of pseudocapacitance using Bode plots as well as the properties of Bode plots are introduced with such an equivalent circuit diagram and corresponding processes.

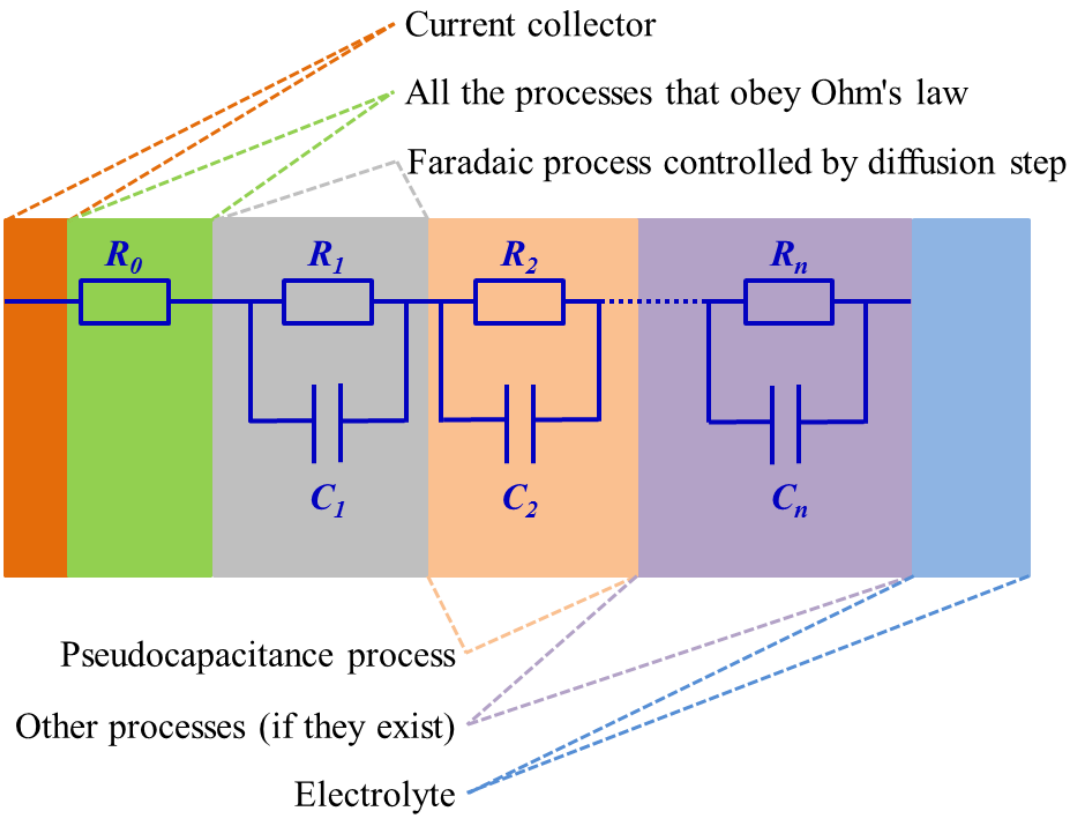

Figure 1. The processes of electrochemical reaction with pseudocapacitance for electrodes.

2. Results and Discussion

2.1 The characteristic differences between Nyquist and Bode plots.

For the equivalent circuit diagram shown inset in Fig. 2, which is composed of two resistances with values of 1 Ω and 1000 Ω and a capacitance whose value varies, the simulated Nyquist plots show no obvious changes with increasing capacitance from 4.7 μF to 47 μF, and, then, to 470 μF. All three curves overlap with each other while the Bode plots indicate regular variations. In addition, peaks are observed in the phase-angle plots, which shift to lower frequency with increasing capacitance. Although the shapes for the modulus of the impedance plots are similar, they also shift with the changing capacitance. Therefore, the main difference between Nyquist and Bode plots is that the Bode plots are much more sensitive to changes in the capacitances compared to the Nyquist plots. Consequently, any change in capacitance will have a much more significant signature in the Bode plots. Thus, Bode plots are more suitable for the discussion of pseudocapacitances and capacitances.

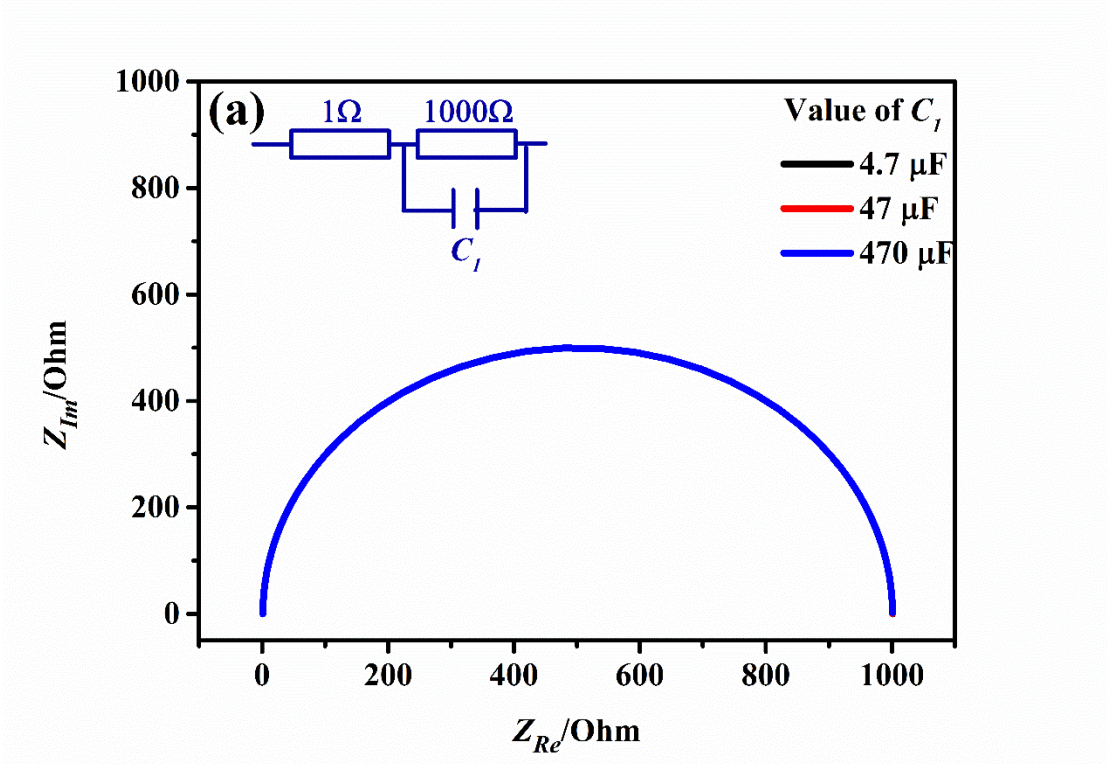

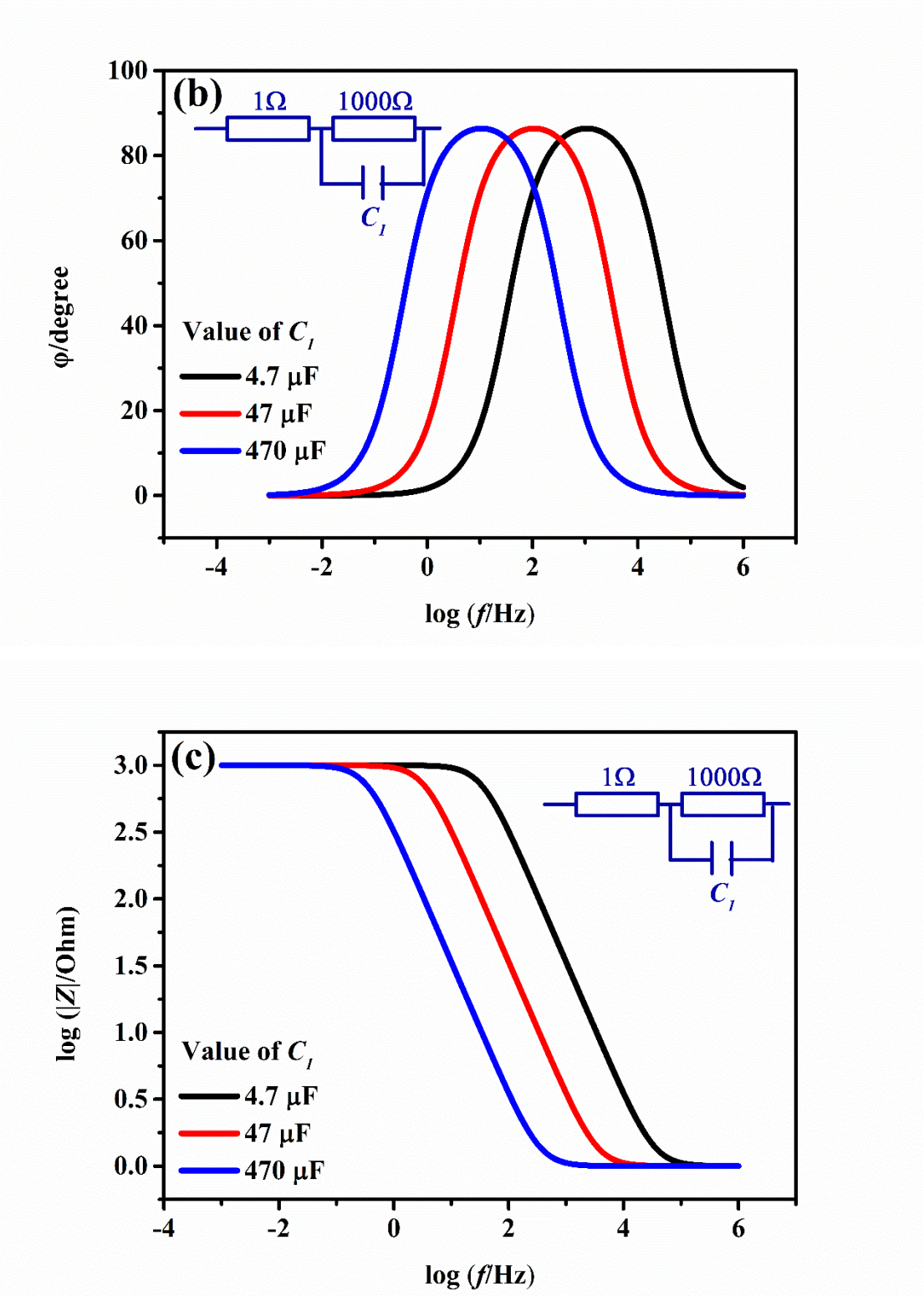

Figure 2. Nyquist plots (a) and phase-angle Bode plots (b), modulus of impedance Bode plots (c) for an equivalent circuit diagram composed of two resistances and one capacitance.

2.2 Properties of Bode plots.

2.2.1 Properties of the single components for the equivalent circuit diagrams.

The impedance *Z*, real part of the impedance Z_{Re}, imaginary part of the impedance Z_{Im}, modulus of the impedance $|Z|$, relationship between impedance modulus and angular frequency $\log|Z|$~$\log\omega$, and the phase angle φ and $\tan\varphi$ for a single resistance R_0 or a single capacitance C_1 are all summarized in Table 1.[34]

Table 1 Parameters of a single component for the equivalent circuit diagrams.

Component	Z	Z_{Re}	Z_{Im}	$\|Z\|$	$\log\|Z\|$~$\log\omega$	φ	$\tan\varphi$
Resistance R_0	R_0	R_0	0	R_0	---	0	0
Capacitance C_1	$-\mathrm{j}\left(\frac{1}{\omega C_1}\right)$	0	$\frac{1}{\omega C_1}$	$\frac{1}{\omega C_1}$	Linear, slope= -1	$\pi/2$	∞

2.2.2 Properties of a simple equivalent circuit diagram.

For the equivalent circuit diagram shown in Fig. 3a, some of its parameters can be expressed using Eq. 1-4.

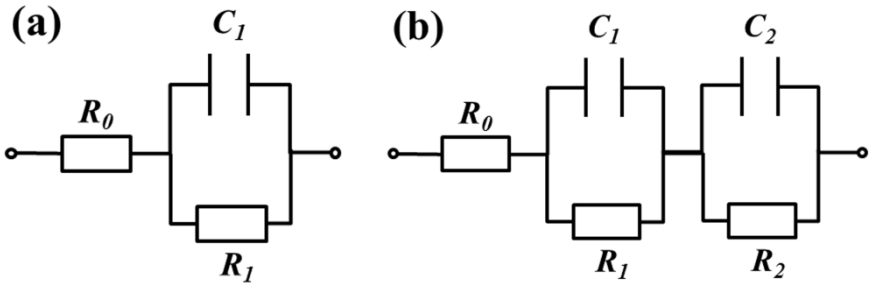

Figure 3. Equivalent circuit diagrams.

$$Z = R_0 + \frac{1}{\frac{1}{R_1} + \frac{1}{\frac{1}{\mathrm{j}\omega C_1}}} = R_0 + \frac{1}{\frac{1}{R_1} + \mathrm{j}\omega C_1} = \frac{R_0 + R_1 + R_0(\omega R_1 C_1)^2}{1 + (\omega R_1 C_1)^2} - \mathrm{j}\frac{\omega R_1^2 C_1}{1 + (\omega R_1 C_1)^2} \quad (1)$$

$$\tan\varphi = -\frac{-\frac{\omega R_1^2 C_1}{1 + (\omega R_1 C_1)^2}}{\frac{R_0 + R_1 + R_0(\omega R_1 C_1)^2}{1 + (\omega R_1 C_1)^2}} = \frac{\omega R_1^2 C_1}{R_0 + R_1 + R_0(\omega R_1 C_1)^2} \quad (2)$$

$$|Z|^2 = Z^2 = R_0^2 + \frac{2R_0 R_1 + R_1^2}{1 + (\omega R_1 C_1)^2} \quad (3)$$

$$\log|Z| = \frac{1}{2}\log[(R_0 + R_1)^2 + (\omega R_0 R_1 C_1)^2] - \frac{1}{2}\log[1 + (\omega R_1 C_1)^2] \quad (4)$$

(1) When ω is so low that $\omega R_1 C_1$ is far smaller than 1, $Z^2 = R_0^2 + 2R_0R_1 + R_1^2$ $(Z = R_0 + R_1)$. In this case, the very small value for ω leads to a large impedance for C_1, which is as large as a breakage appearing in the branch circuit of C_1, which is effectively the same as saying no C_1 is present in the equivalent circuit diagram.

(2) When ω is so high that $\frac{2R_0R_1+R_1^2}{1+(\omega R_1 C_1)^2}$ approaches 0, Z equals R_0. Under this circumstance, R_1 is short-circuited, as a very high ω for C_1 results in an impedance that is as small as that found in an ordinary wire, leaving only R_0 functioning well.

(3) When ω is in a proper range (neither too high nor too low), the properties of the equivalent circuit diagram shown in Fig. 3a depend on the relative impedance values for R_0 and R_1.

When the impedance for R_0 is much smaller than the total impedance of the entire equivalent circuit diagram, i.e., R_0 is negligible, the properties of the equivalent circuit diagram can be summarized by Eq. 5-8.

$$Z = \frac{1}{\frac{1}{R_1} + \frac{1}{\frac{1}{j\omega C_1}}} = \frac{1}{\frac{1}{R_1} + j\omega C_1} = \frac{R_1}{1 + (\omega R_1 C_1)^2} - j\frac{\omega R_1^2 C_1}{1 + (\omega R_1 C_1)^2} \quad (5)$$

$$\tan\varphi = -\frac{-\frac{\omega R_1^2 C_1}{1 + (\omega R_1 C_1)^2}}{\frac{R_1}{1 + (\omega R_1 C_1)^2}} = \omega R_1 C_1 \quad (6)$$

$$|Z|^2 = Z^2 = \frac{R_1^2}{1 + (\omega R_1 C_1)^2} \quad (7)$$

$$\log|Z| = \log R_1 - \frac{1}{2}\log[1 + (\omega R_1 C_1)^2] \quad (8)$$

(3a) When ω is relatively low and $\omega R_1 C_1 \ll 1$, $\log|Z|$ in Eq. 8 is close to $\log R_1$, $|Z| \approx R_1$. Therefore, when ω is relatively low and R_0 is very small, the equivalent circuit diagram shows properties similar to that found for a single resistance R_1.

(3b) When ω is relatively high so that $\omega R_1 C_1 \gg 1$, $|Z|^2$ in Eq. 7 is approximately equal to $\frac{R_1^2}{(\omega R_1 C_1)^2}$, $|Z| = \frac{1}{\omega C_1}$. Therefore, when ω is relatively high and R_0 is very small, the equivalent circuit

properties become similar to that expected for a single capacitance C_1.

When R_1 is sufficiently large enough, the branch circuit with R_1 is disconnected, the properties of the equivalent circuit diagram can be expressed using Eq. 9-12.

$$Z = R_0 + \frac{1}{\mathrm{j}\omega C_1} = R_0 - \mathrm{j}\frac{1}{\omega C_1} \quad (9)$$

$$\tan\varphi = \frac{-\left(-\frac{1}{\omega C_1}\right)}{R_0} = \frac{1}{\omega R_0 C_1} \quad (10)$$

$$|Z|^2 = Z^2 = \frac{1 + (\omega R_0 C_1)^2}{(\omega C_1)^2} \quad (11)$$

$$\log|Z| = \frac{1}{2}\log[1 + (\omega R_0 C_1)^2] - \log\omega - \log C_1 \quad (12)$$

(3c) When ω is relatively low and $\omega R_0 C_1 \ll 1$, $|Z|^2$ in Eq. 11 is roughly equal to $\frac{1}{(\omega C_1)^2}$, so $|Z| = \frac{1}{\omega C_1}$. In other words, when ω is relatively low and R_1 is very large, the equivalent circuit diagram properties become similar to that expected for a single capacitance C_1 (This can also be proven using $\log|Z| \approx \log\frac{1}{\omega C_1}$ in Eq. 12).

(3d) When ω is relatively high to satisfy the condition $\omega R_0 C_1 \gg 1$, $|Z|^2$ in Eq. 11 approaches R_0^2. The equivalent circuit diagram shows properties similar to that of a single resistance R_0 when ω is relatively high and R_1 is very large.

Properties of the equivalent circuit diagram shown in Fig. 3a are summarized in Table 2. Its theoretical Bode plots within the proper frequency range are shown in Fig. 4, in which f is the frequency, $\omega = 2\pi f$.

Table 2 Parameters for the equivalent circuit diagram shown in Fig. 3a.

Parameters	Angular Frequency (ω)/ Frequency (f)				
	Extremely low	Proper range			Extremely high
		Very small R_0		Very large R_1	
		Relatively low	Relatively high	Relatively low	Relatively high

	(1)	(3a)	(3b)	(3c)	(3d)	(2)
Z	R_0+R_1	R_1	$-\mathrm{j}\left(\frac{1}{\omega C_1}\right)$	$-\mathrm{j}\left(\frac{1}{\omega C_1}\right)$	R_0	R_0
Z_{Re}	R_0+R_1	R_1	---	---	R_0	R_0
Z_{Im}	---	---	$\frac{1}{\omega C_1}$	$\frac{1}{\omega C_1}$	---	---
$\lvert Z\rvert$	R_0+R_1	R_1	$\frac{1}{\omega C_1}$	$\frac{1}{\omega C_1}$	R_0	R_0
$\log\lvert Z\rvert\sim\log\omega$	---	---	Linear, slope=-1	Linear, slope=-1	---	---
φ	0	0	π/2	π/2	0	0
$\tan\varphi$	0	0	∞	∞	0	0

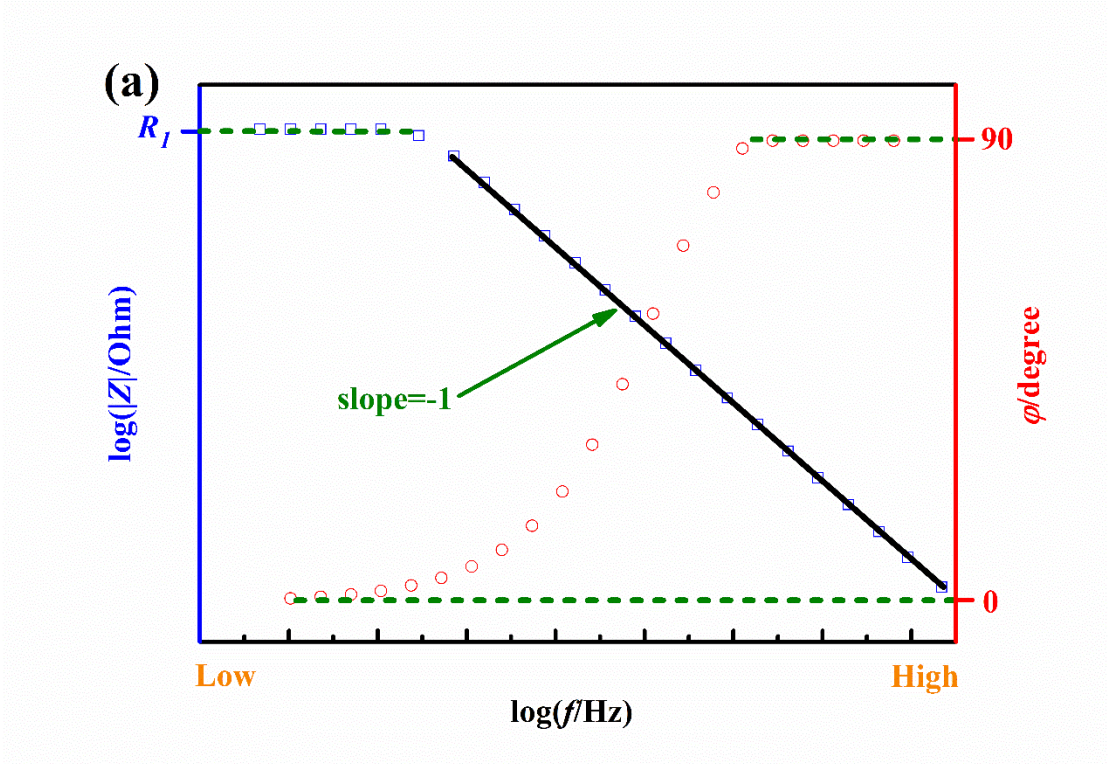

10.1002/celc.201900289

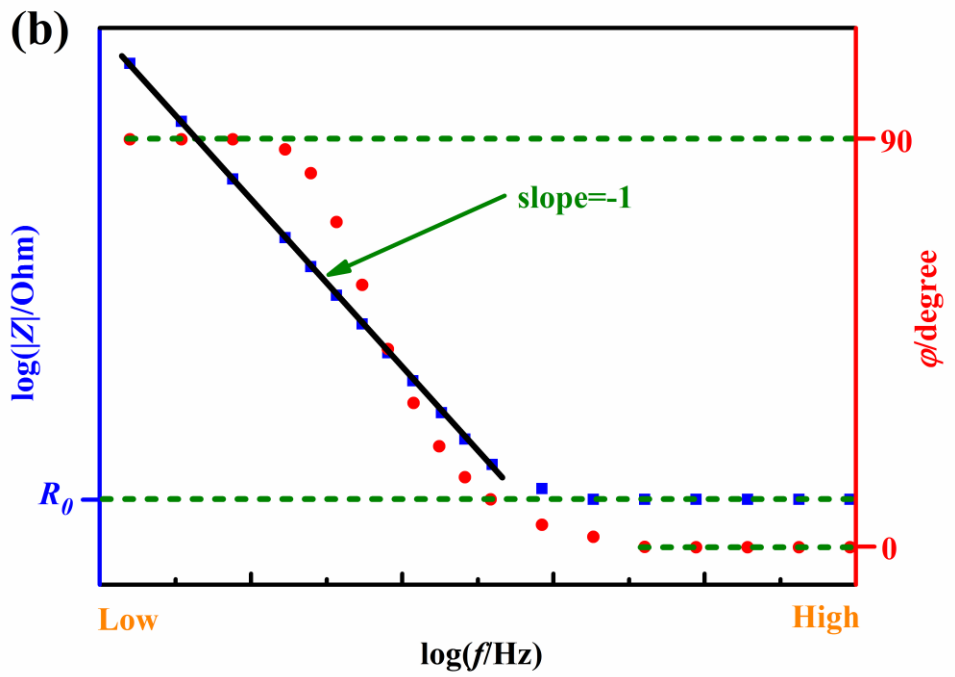

Figure 4. Fitting Bode plots within a proper frequency range for the equivalent circuit diagram shown in Fig. 3a for very small R_0 (a) and very large R_1 (b). f is frequency, $\omega = 2\pi f$.

In summary, theoretical Bode plots for the equivalent circuit diagram shown in Fig. 3a should be shaped as in Fig. 5. In the middle frequency range, an intermediate zone exists (marked with dashed box), which shows a sign of a peak at 90 °in the theoretical phase-angle Bode plots and a line with a slope of -1 in the theoretical impedance module Bode plots. For comparison, the practical situation was revealed using EC-Lab by setting R_0=100 Ω, R_1=1000 Ω, C_1=470 μF. As shown in Fig. 5, a peak in the practical phase-angle Bode plot and a single line in the practical impedance module Bode plot were generated, which is in accordance with the theoretical derivation. For the condition in which R_0 is negligible and R_1 cannot work efficiently, one obtains 90 °and -1 for the values of the peak angle and slope, respectively. Thus, it is normal for the practical values to slightly deviate from the theoretical values.

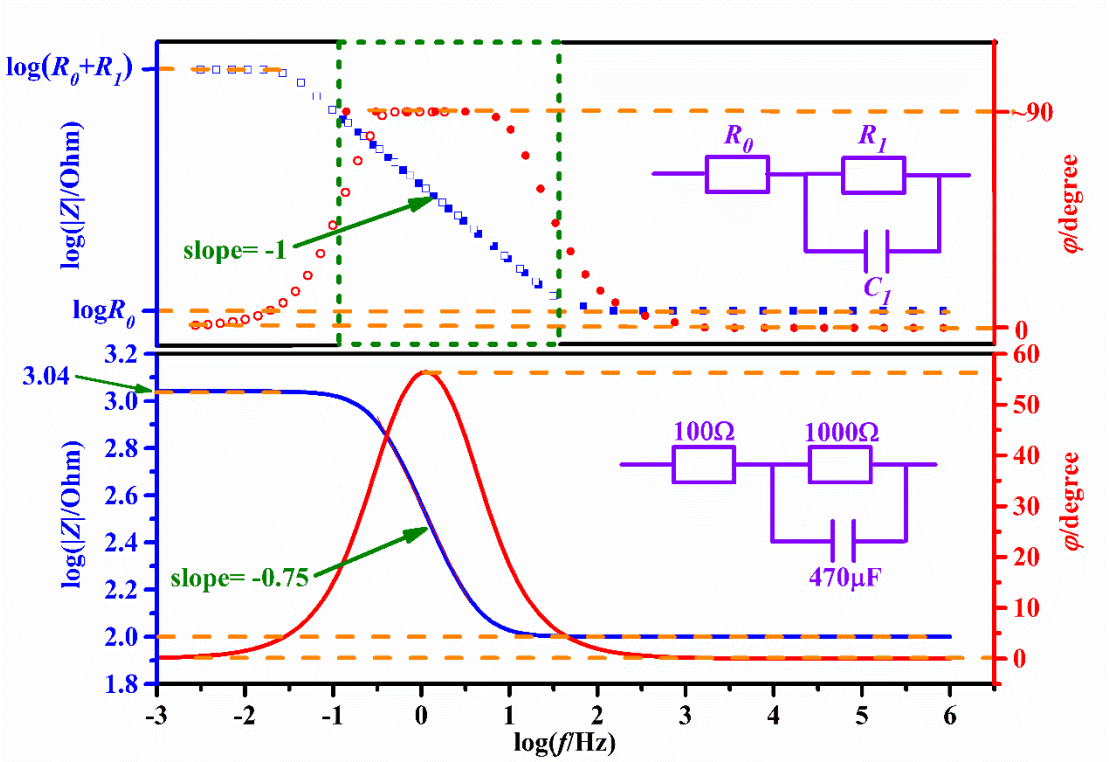

Figure 5. Theoretical and practical Bode plots of equivalent circuit diagram shown in Fig. 3a.

2.2.3 Properties of the complex equivalent circuit diagram.

The impedance of the circuit diagram shown in Fig. 3b is expressed as Eq. 13. Its Nyquist and Bode plots are also shown in Fig. 6.

$$Z = R_0 + \frac{R_1}{1+(\omega R_1 C_1)^2} + \frac{R_2}{1+(\omega R_2 C_2)^2} - \mathrm{j}\left[\frac{\omega R_1^2 C_1}{1+(\omega R_1 C_1)^2} + \frac{\omega R_2^2 C_2}{1+(\omega R_2 C_2)^2}\right] \qquad (13)$$

With R_0=1 Ω, R_1=10 Ω, R_2=1000 Ω, C_1=470 μF and C_2 varying from 100 μF to 1000 μF, and, then, to 10000 μF, the Nyquist plots show little difference, as shown in Fig. 6a. While in Fig. 6b, c, both Bode plots show obvious changes. Compared to the impedance modulus of impedance Bode plots, the phase-angle Bode plots showed a much more complicated evolution. When C_2=100 μF, only one wide peak is observed. The Peaks begin to divide as C_2 is increased to 1000 μF. Not until C_2=10000 μF do the two individual peaks show complete shapes. From a comparison between Nyquist plots, impedance module Bode plots and phase-angle Bode plots, the phase-angle Bode plots were found to be the most suitable for revealing changes in capacitances directly and sensitively as they show 3 shapes quite distinct from each other. The evolution of the peaks in the

phase-angle Bode plots indicate that the wider and more numerous the peaks, the more capacitive features exist, demonstrating the existence of pseudocapacitance.

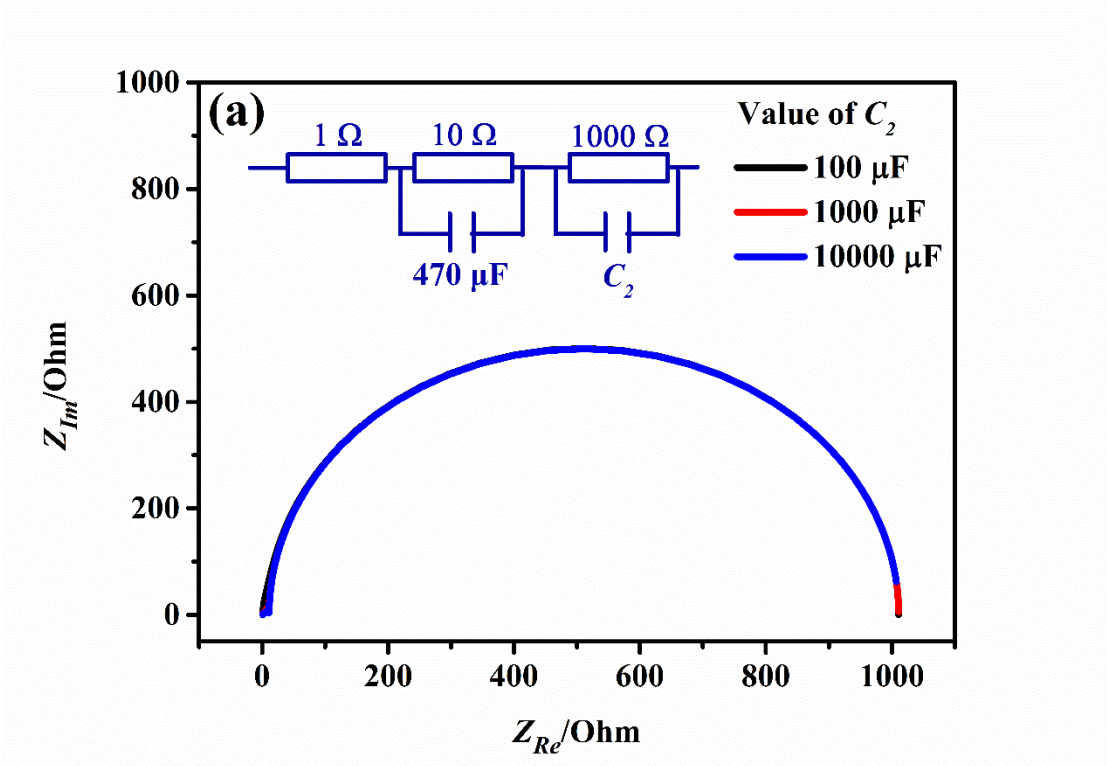

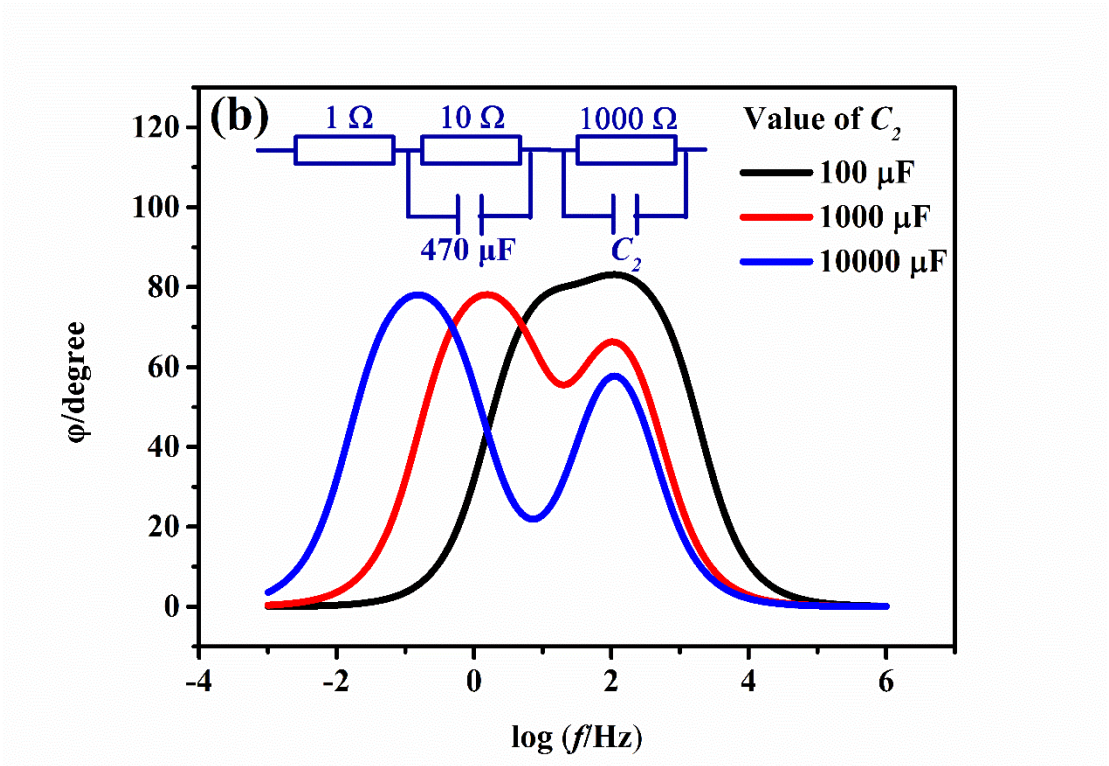

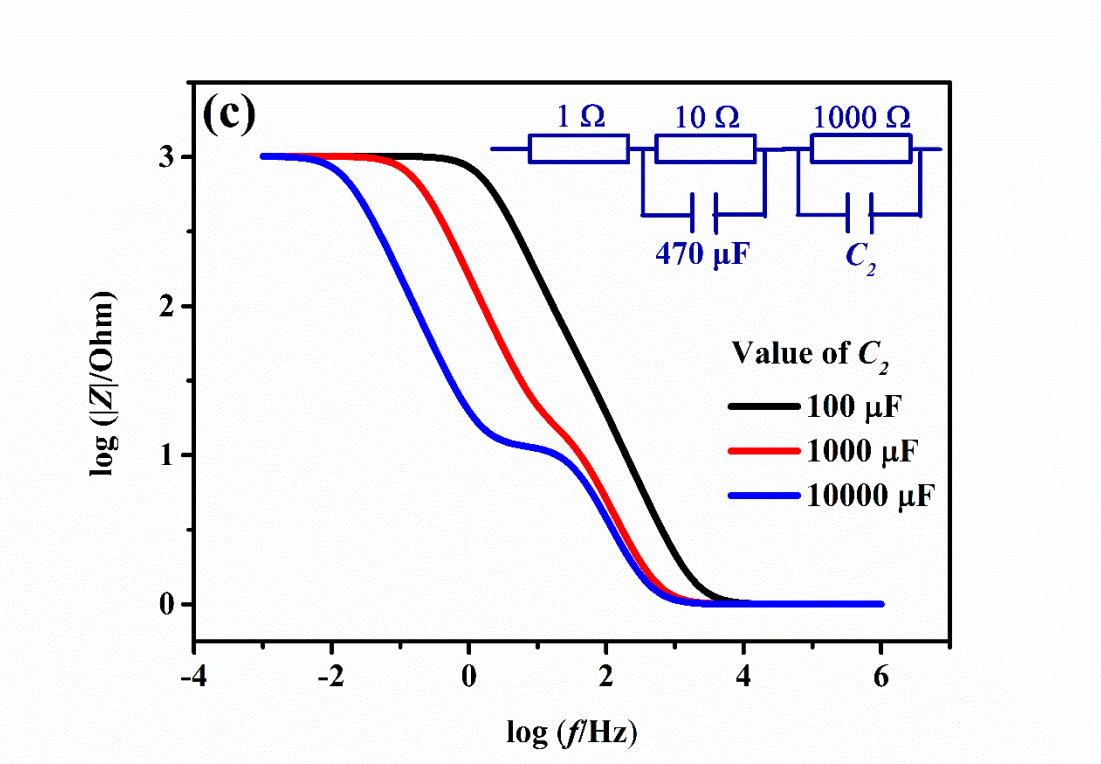

Figure 6. Nyquist plots (a), phase-angle Bode plots (b) and impedance module Bode plots (c) for the equivalent circuit diagram shown in Fig. 3b.

2.3 Usage of Bode plots to demonstrate the existence of pseudocapacitance.

TEM images in Fig. 7 display the morphology of Co_3O_4. Instead of agglomerating, particles with diameter about 30 nm form three-dimensional interconnected structure, and porous and void structures are observed.

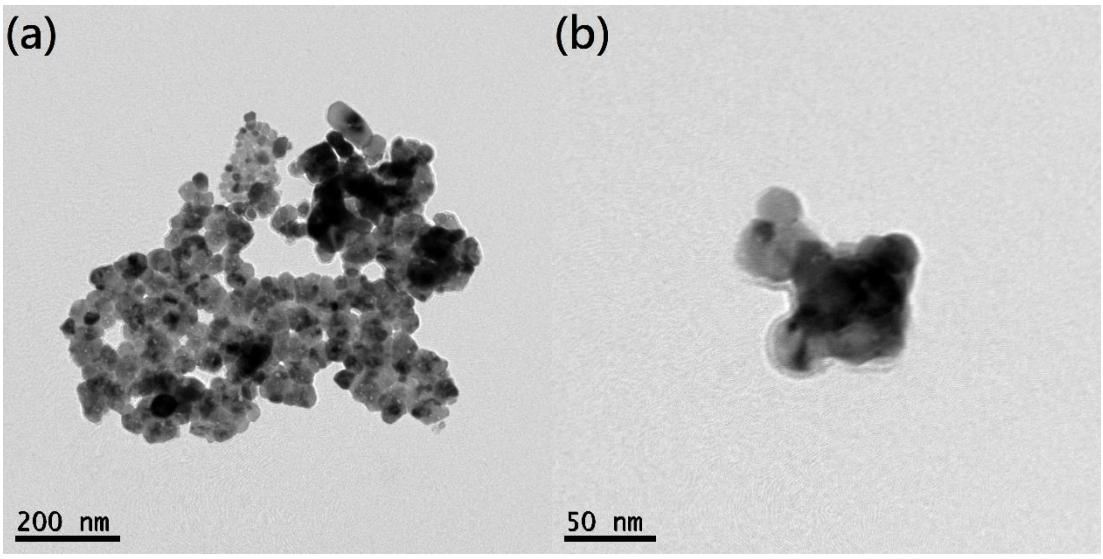

10.1002/celc.201900289

Figure 7. TEM images of Co_3O_4.

The Co_3O_4 samples utilized in this discussion exhibit reversible specific capacities exceeding the theoretical value (890 mAh g^{-1})[35] for 16 cycles at 0.05 mA cm^{-2}, as shown in Fig. 8a, which can be attributed to the contribution of pseudocapacitance, as mentioned in the introduction. As the solid electrolyte interface (SEI) turns out to be stabilized after galvanostatic charging and discharging for 5 cycles,[36, 37] the EIS test was conducted after charging and discharging the testing battery with 0.05 mA cm^{-2} for 5 cycles. The phase-angle Bode plots (for the fully charged state, 3 V vs. Li^+/Li) are shown as Fig. 8b.

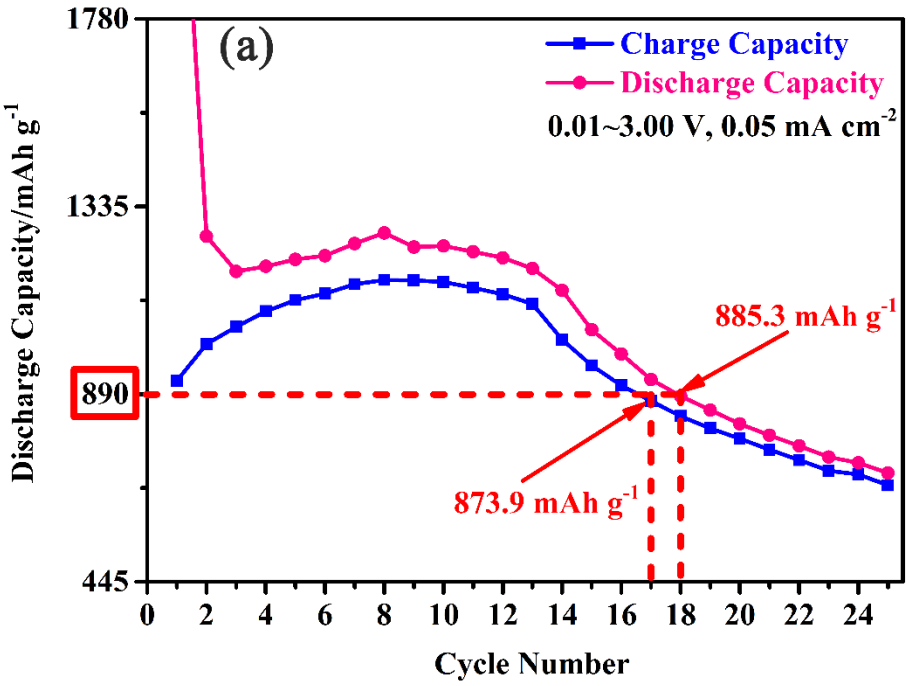

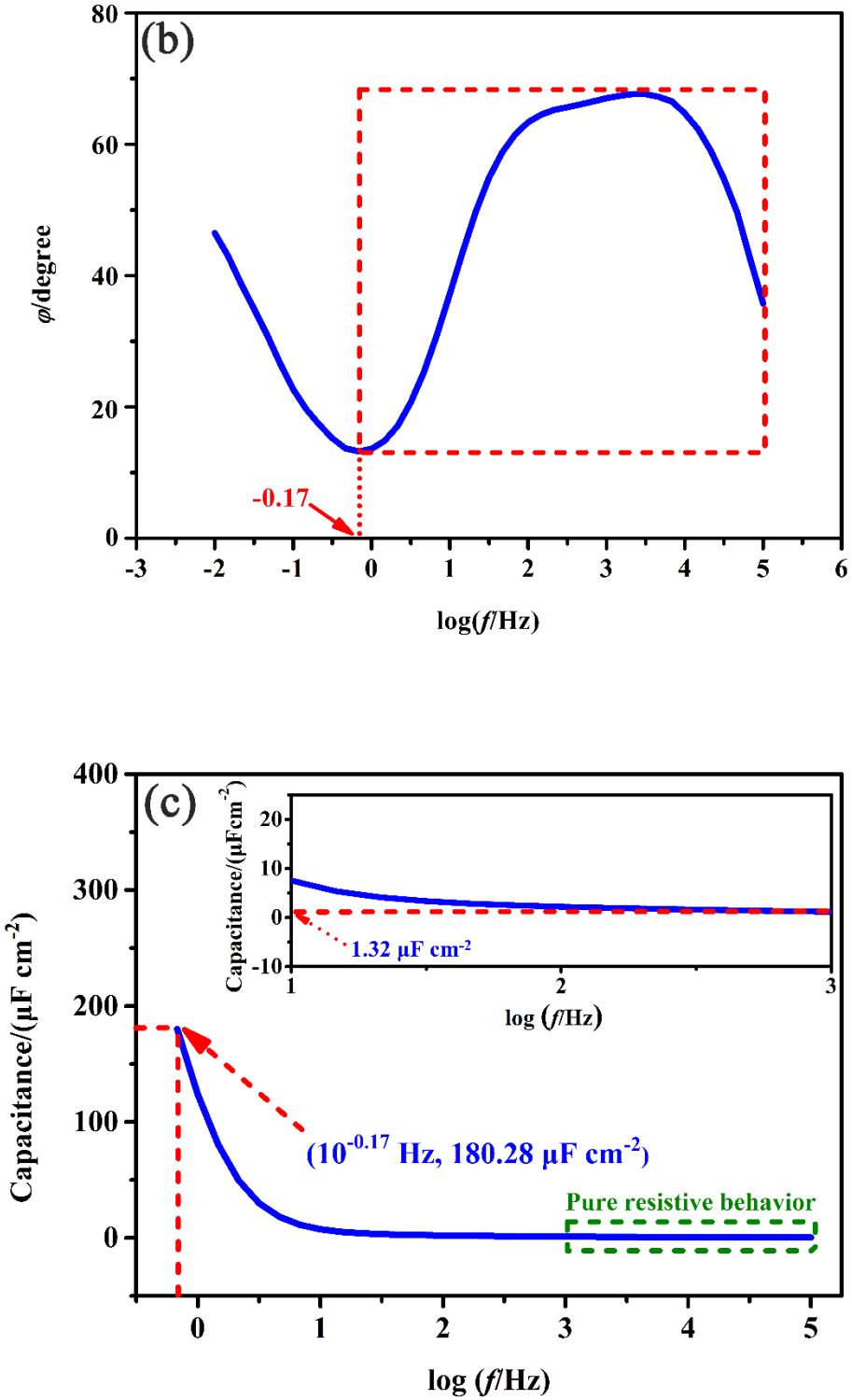

Figure 8. Specific capacities at 0.05 mA cm^{-2} for the initial 25 cycles (a), phase-angle Bode plot (b) and double layer capacitance and pseudocapacitance (c) for Co_3O_4.

The phase-angle Bode plot for Co_3O_4 shows that within the relative high-frequency region ($10^{-0.17}$~10^5 Hz, marked with a dashed box in Fig. 8b), in which the non-diffusion controlled processes take place, one wide peak appears that occupies the whole high frequency region. Such wide peaks demonstrate the existence of pseudocapacitance. According to Table 2 and previous studies of capacitive properties,[38-40] Eq. 14 can be used to calculate the values for C_n (n=1,2) in the corresponding frequency ranges. Thus, the double layer capacitance and pseudocapacitance can be calculated using Z_{Im} and ω, as shown in Fig. 8c.

$$Z_{Im} = \frac{1}{\omega C_n} \ (n = 1, 2) \tag{14}$$

As shown in Fig. 8c, the capacitance starts decreasing from 180.28 μF cm^{-2} at ~0.68 ($10^{-0.17}$) Hz, and, then, becomes stable at 1.32 μF cm^{-2} at a frequency higher than 100 Hz. For frequencies higher than 1000 Hz, the capacitance approaches 0, indicating purely resistive behavior. Thus, within the relatively high-frequency region ($10^{-0.17}$~10^5 Hz, marked with a dashed box in Fig. 8b), in which the non-diffusion controlled processes take place, the pseudocapacitance and double layer capacitance for Co_3O_4 in the fully charged state is approximately 180.28 μF cm^{-2} and 1.32 μF cm^{-2}, respectively.

Particles in nano-scale possess more surfaces, which compose electrode with high surface areas. Thus, higher double layer capacitance is achieved. As the pseudocapacitance involves charge storage based on continuous, fast, and reversible redox reactions occurring at the surface of electrode, higher pseudocapacitance is also observed in electrode with high surface areas.

3. Conclusion

To emphasize the pseudocapacitive behavior of transition metal oxides using Co_3O_4 as an example, the electrochemical reaction processes were divided into at least 4 component parts, including processes that follow Ohm's law, a faradic process controlled by solid phase diffusion, a pseudocapacitive process and other possible phenomena. Taking each part into consideration, a corresponding equivalent circuit diagram was built. After analyzing the properties of the Bode plots

in the whole frequency range (10^{-2}~10^{5} Hz), phase-angle Bode plots were demonstrated to be suitable for revealing the pseudocapacitance of Co_3O_4 in a certain state. In addition, $C = 1/(\omega Z_{Im})$ was employed to determine the magnitude of the pseudocapacitance and double layer capacitance. For Co_3O_4 with the fully charged state (3 V vs. Li^+/Li), the pseudocapacitance and double layer capacitance is approximately 180.28 μF cm^{-2} and 1.32 μF cm^{-2}, respectively.

The analysis of the Bode plots and summary of their features here provides a possible approach to precisely monitor pseudocapacitive behavior for a transition metal oxide anode, as one can rule out the double layer capacitance on the basis of separating out all the capacitive behavior due to faradaic processes controlled by solid phase diffusion, boosting the understanding and controllable application of pseudocapacitance as well as the development of electrode materials with multi-storage mechanisms for lithium ion batteries. Therefore, the introduction of Bode plots for monitoring pseudocapacitive behavior in lithium ion batteries can be used to develop new electrochemical technology and is a promising direction for the further progression of lithium ion batteries.

4. Experimental Section

4.1 Fabrication and characterization of Co_3O_4.

First, 0.01 mol cobalt chloride hexahydrate ($CoCl_2$ $6H_2O$, ≥99.9%，Sinopharm Chemical Reagent Co., Ltd.) was dissolved into 500 mL deionized water. Then, 0.1 mol L^{-1} oxalic acid ($C_2H_2O_4$, ≥99%, Sinopharm Chemical Reagent Co., Ltd.) was added with continuous stirring. After reacting for 3 hours, the pink solution was vacuum filtered to obtain CoC_2O_4 microrods as a pink solid. They were washed with deionized water several times, and the pink solid was dissolved into 250 mL ethanol (C_2H_6O, ≥99.7%, Sinopharm Chemical Reagent Co., Ltd.). Two hundred fifty milliliters of a 0.1 mol L^{-1} sodium hydroxide (NaOH, ≥97%, Sinopharm Chemical Reagent Co., Ltd.) solution in ethanol was added with continuous stirring. Once the solution of sodium hydroxide in ethanol was added dropwise to the suspension, the Kirkendall effect started to play a pivotal role. Throughout the 3 hours reaction, continuous ionic migration at different rates proceeded at the solid-liquid interface.

As a result of the rapid formation of an interconnected $Co(OH)_2$ shell over the external surface of CoC_2O_4 microrods allowed the outer shell to prevent direct reaction between Co^{2+} and OH^-. The

following reaction relies on the diffusion rates of Co^{2+} and OH^- through the $Co(OH)_2$ shell. Faster outward diffusion of Co^{2+} through the $Co(OH)_2$ shell resulted in inner void spaces, and the migration of ions created pores in the shells. Finally, after being washed with deionized water and ethanol several times and placed in a circulation oven at 50 ℃ for 24 hours, the precursor was calcined at 350 ℃ for 3 hours (heating rate 1 ℃ min^{-1}) to obtain Co_3O_4 microtubes with balsam pear-shaped outer surface and void spaces in the walls.[41]

The morphology was observed by transmission electron microscopy (TEM, Philips CM12).

4.2 Electrochemical measurements for test batteries.

Testing cells were fabricated utilizing the active materials with acetylene black and polyvinylidene difluoride (PVDF) as the working electrode with a surface area of ~1.77 cm^2 (diameter of 15 mm and thickness of 250 μm). In detail, active material (70 wt.%), acetylene black (20 wt.%) and PVDF binder (10 wt.%) were dispersed in N-methyl-2-pyrrolidinone (NMP) solvent, and, then, stirred thoroughly to form a slurry. The slurry was spread onto copper foil and maintained at 120 ℃ in an oven overnight. Approximately 1.6 mg of active materials was deposited onto each working electrode. A metallic lithium plate was used as the counter electrode. Celgard 2400 was used as a separator. The electrolyte was 1 mol L^{-1} $LiPF_6$ in a 1:1 (volume ratio) mixture of ethylene carbonate (EC) and dimethyl carbonate (DMC).

EIS tests were conducted in the fully charged state (3 V vs. Li^+/Li) using a VMP3 (Biologic) electrochemical workstation with a frequency range of 10^5~10^{-2} Hz using a sine wave of 5 mV in the charged state (3 V vs. Li^+/Li) of the testing batteries. Galvanostatic charging and discharging was evaluated using an Arbin BT2000 multichannel galvanostat in the potential range of 0.01~3.00 V (vs. Li/Li^+) at 0.05 mA cm^{-2}.

4.3 Software simulation of Nyquist and Bode plots.

In the exploration of properties for different equivalent circuit diagrams, Nyquist and Bode plots were simulated using "EC-Lab" software (Version 11.10). In particular, Nyquist and Bode plots were simulated using the "ZSim" function for "Electrochemical Impedance Spectroscopy" under the menu "Analysis", with a frequency range of 10^6~10^{-3} Hz, "20 points per decade in logarithm spacing" and certain values for the components in the equivalent circuit diagrams.

References:

[1] A. G. Dylla, G. Henkelman, K. J. Stevenson, *Accounts Chem. Res.* **2013**, 46, 1104-1112.

[2] Y. F. Zhukovskii, P. Balani, E. A. Kotomin, M. Joachim, *Phys. Rev. Lett.* **2006**, 96, 058302.

[3] J. Wang, J. Polleux, J. Lim, B. Dunn, *J. Phys. Chem. C* **2007**, 111, 14925-14931.

[4] P. Ge, S. Li, H. Shuai, W. Xu, Y. Tian, L. Yang, G. Zou, H. Hou, X. Ji, *Nano Energy* **2018**, 54, 26-38.

[5] P. Balaya, A.J. Bhattacharyya, J. Jamnik, *J. Power Sources* **2006**, 159, 171-178.

[6] J. Jamnik, J. Maier, *Phys. Chem. Chem. Phys.* **2003**, 5, 5215-5220.

[7] F. Shi, D. Xie, Y. Zhong, D. H. Wang, X. H. Xia, C. D. Gu, X. L. Wang, J. P. Tu, *J. Power Sources* **2016**, 327, 281-288.

[8] Y. Zhu, Z. Huang, Z. Hu, L. Xi, X. Ji, Y. Liu, *Electrochim. Acta* **2018**, 269, 30-37.

[9] B. E. Conway, V. Birss, J. Wojtowicz, *J. Power Sources* **1997**, 66, 1-14.

[10] F. Fan, S. Zhao, R. Rui, Z. Yang, Q. Shen, *Electrochim. Acta* **2016**, 222, 1160-1168.

[11] S. Liu, S. Sun, X. You, *Nanoscale* **2014**, 6, 2037-2045.

[12] F. Shi, L. Li, X. Wang, C. Gu, J. Tu, *Rsc Adv.* **2014**, 4, 41910-41921.

[13] C. D. Lokhande, D. P. Dubal, O. S. Joo, *Curr. Appl. Phys.* **2011**, 11, 255-270.

[14] J. Jiang, Y. Li, J. Liu, X. Huang, C. Yuan, X. Lou, *Adv. Mater.* **2012**, 24, 5166-5180.

[15] V. Aravindan, J. Gnanaraj, Y. S. Lee, S. Madhavi, *Chem. Rev.* **2014**, 114, 11619-11635.

[16] X. Zhang, Z. Yang, C. Li, A. Xie, Y. Shen, *Appl. Surf. Sci.* **2017**, 403, 294-301.

[17] X. Wang, B. Zhou, J. Guo, W. Zhang, X. Guo, *Mater. Res. Bull.* **2016**, 83, 414-422.

[18] C. Yan, G. Chen, J. Sun, X. Zhou, C. Lv, *Phys. Chem. Chem. Phys.* **2016**, 18, 19531-19535.

[19] T. Li, X. Li, Z. Wang, H. Guo, Q. Hu, W. Peng, *Electrochim. Acta* **2016**, 209, 456-463.

[20] W. Xu, Z. Xie, X. Cui, K. Zhao, L. Zhang, L. Mai, Y. Wang, *J. Mater. Chem. A* **2016**, 4, 3735-3742.

[21] G. Fang, J. Zhou, C. Liang, A. Pan, C. Zhang, Y. Tang, X. Tan, J. Liu, S. Liang, *Nano Energy* **2016**, 26, 57-65.

[22] X. Yao, G. Guo, Y. Zhao, Y. Zhang, S. Tan, Y. Zeng, R. Zou, Q. Yan, Y. Zhao, *Small* **2016**, 12, 3849-3860.

[23] Y. Tan, Q. Gao, Z. Li, W. Tian, W. Qian, C. Yang, H. Zhang, *Sci. Rep.* **2016**, 6, 26460.

[24] X. Hou, H. Jian, K. An, J. Mu, X. Chou, C. Xue, *Appl. Surf. Sci.* **2016**, 383, 159-164.

[25] W. Gou, X. Zhou, J. Li, Y. Ma, *Mater. Lett.* **2016**, 180, 207-211.

[26] Q. Li, H. Wang, J. Ma, X. Yang, R. Yuan, Y. Chai, *J. Alloy. Compd.* **2018**, 735, 840-846.

[27] N. Shen, M. Keppeler, B. Stiaszny, H. Hain, F. Maglia, M. Srinivasan, Beilstein *J. Nanotechnol.* **2017**, 8, 2032-2044.

[28] Y. Wang, J. Han, X. Gu, S. Dimitrijev, Y. Hou, S. Zhang, *J. Mater. Chem. A* **2017**, 5, 18737-18743.

[29] Y. Zhao, X. Zhai, Y. Dong, C. Ding, N. Wu, D. Su, Y. Zhao, H. Zhou, X. Zhao, J. Li, H. Jin, *Electrochim. Acta* **2017**, 243,18-25.

[30] X. Zhu, X. Jiang, X. Chen, X. Liu, L. Xiao, Y. Cao, *J. Alloy. Compd.* **2017**, 711, 15-21.

[31] P. Balaya, H. Li, L. Kienle, J. Maier, *Adv. Funct. Mater.* **2010**, 13, 621-625.

[32] G. Sudant, E. Baudrin, D. Larcher, J. M. Tarascon, *J. Mater. Chem.* **2005**, 15, 1263-1269.

[33] H. Hou, C. E. Banks, M. Jing, Y. Zhang, X. Ji, *Adv. Mater.* **2015**, 27, 7861-7866.

[34] A. J. Bard, L. R. Faulkner, Electrochemical methods: fundamentals and applications. New York: Wiley, 1980.

[35] M. Xu, F. Wang, Y. Zhang, S. Yang, M. Zhao, X. Xiong, *Nanoscale* **2013**, 5, 8067-8072.

[36] H. Bryngelsson, M. Stjerndahl, T. Gustafsson, K. Edström, *J. Power Sources* **2007**, 174, 970-975

[37] D. Alliata, R. Kötz, P. Novák, H. Siegenthaler, *Electrochem. Commun.* **2000**, 2, 436-440.

[38] S. Patanè, C. Triolo, P. Cardiano, S. L. Schiavo, *Ionics* **2017**, 23, 1481-1487

[39] C. W. Liew, S. Ramesh, A. K. Arof, *Int. J. Hydrogen Energ.* **2014**, 39, 2953-2963.

[40] S. Mitra, A. K. Shukla, S. Sampath, *J. Power Sources* **2001**, 101, 213-218.

[41] Z. Yang, S. Wang, Y. Liu, X. Lei, *Ionics* **2015**, 21, 2423-2430.

10.1002/celc.201900289

Keywords: pseudocapacitance • double layer capacitance • cobaltosic oxide • transition metal oxide • lithium ion batteries